2018-06

Offshore monopile in the southern North Sea: part II, simulated hydrodynamics and loading

Edesess, Ariel

10.1680/jmaen.2018.16
Proceedings of the Institution of Civil Engineers - Maritime Engineering
Thomas Telford Ltd.

Accepted manuscript doi:
10.1680/jmaen.2018.16

Accepted manuscript doi:
10.1680/jmaen.2018.16

Submitted: 02 May 2018

Published online in 'accepted manuscript' format: 09 August 2018

Manuscript title: Offshore monopile in the southern North Sea: Part II, simulated hydrodynamics and loading

Authors: Ariel J. Edesess[1], Denis Kelliher[1], Alistair G. L. Borthwick[2] and Gareth Thomas[3]

Affiliations: [1]Department of Civil and Environmental Engineering, University College Cork, College Road, Cork, Ireland; [2]School of Engineering, The University of Edinburgh, The King's Buildings Edinburgh, EH9 3JL, UK; [3]Department of Applied Mathematics, Western Gateway Building, Western Road, University College Cork, Cork, Ireland

Corresponding author: Ariel J. Edesess, Department of Civil and Environmental Engineering, University College Cork, College Road, Cork, Ireland. Tel.: 00353851464676.

E-mail: a.edesess@umail.ucc.ie

Accepted manuscript doi:
10.1680/jmaen.2018.16

Abstract

This paper considers two methods for determining the local wave particle kinematics and hydrodynamic forces on an idealised wind turbine monopile in the southern North Sea using sea state data at Teesside Offshore Wind farm. An assessment of local flow hydrodynamics is important with regard to safe access of personnel from a crew transfer vessel to a monopile. The hydrodynamic behaviour is calculated using an analytical solution from linear diffraction theory and numerical predictions using OpenFOAM, with both slip and no-slip cylinder boundary conditions. Provided the underlying sea state is unidirectional, it is found that close agreement is obtained between analytical and numerical spectra derived from the time series of local free surface elevation, water particle velocity components, and in-line wave force loading on the monopile. Less satisfactory agreement is achieved with sea states possessing a bimodal spectrum, which suggests that bimodal spectra may not be unidirectional.

Keywords: offshore wind farm maintenance / free surface flow / significant wave height / spectral analysis / ocean wave statistics / renewable energy / crew transfer vessel / OpenFOAM® / waveFoam

Accepted manuscript doi:
10.1680/jmaen.2018.16

1. Introduction

Safe access to offshore wind turbine monopiles is of crucial importance to reduce the total energy cost of offshore wind power. Operation and maintenance (O & M) of offshore wind turbines can be 3-5 times the cost of maintenance of onshore wind turbines (IRENA, 2016). Overall, O & M of offshore wind farms account for 25-50% of the total energy cost (Maples et al., 2013; Kostecki, 2014; Dalgic et al., 2015a). Fixed monopile offshore wind turbines make up 80% of offshore wind turbine types (IEA, 2013), and the marine environment adds considerably to the complexity of maintenance of offshore wind turbines in comparison to onshore wind turbines. At present, offshore wind farms are usually located 2-50 km from the shore or onshore base, in water up to 30 m deep (Corbetta et al., 2014; Sperstad et al., 2014). In addition to the cost of parts needed for repairs and economic losses due to wind turbine downtime, it is expensive to hire repair workers and vehicles transporting such workers to the wind farm. Access may be by helicopter, service operations vessel (SOV) or crew transfer vessel (CTV). Smaller CTVs, such as monohulls, catamarans, or Small Waterplane Area Twin Hull (SWATH) type vessels, are the most economic and account for 40.6% of turbine access methods (Dalgic et al., 2015b).

CTV access to offshore wind turbines can be difficult even when the wind farm is located near-shore; it was estimated recently that offshore wind turbines in a wind farm off the coast of Ireland are only accessible for repair 50-75% of a given year (Breton and Moe, 2009; van Bussel et al., 2001). In the context of global offshore wind farm capacity, Dalgic et al. (2015b) report that access for repairs on average is only available 200 days of the year, which reduces in areas with harsher climates. Extreme weather andsea conditions limit access, with most CTV types making the journey only when the significant wave height $H_s \leq$ 1.5 m. However, H_s is an observational parameter and provides no supplementary details about the local water particle kinematics affecting the loading on the turbine monopile, particularly during the time a CTV carrying repair workers is directed against the turbine for access purposes. Furthermore, there is no agreed method or regulation for determining H_s; a survey conducted by Hoffman (2011) found that 49 different models for maintenance strategies and specification of H_s were used by the various offshore wind energy companies.

The unpredictability of sea conditions around the turbine support column can endanger the safety of crew members and the stability of the CTV during crew transfer to the turbine monopile. Contact between the CTV and the turbine support monopile depends on friction between the fender of the CTV and the transition piece on the monopile whilst the CTV is under loading from ocean waves interacting with the monopile. The wave-structure interaction is complex and can vary with changing sea and local hydrodynamic conditions.

This contact is maintained through a steady thrust from the CTV motor throughout crew transfer. If the hydrodynamic force incident on the vessel overcomes the frictional force, the CTV can experience slippage, during which the vessel loses contact with the turbine or undergoes unanticipated motion (Josse et al., 2011; König et al., 2017; Edesess et al. 2017). When vessel slippage occurs, the repair workers are in potential danger and the possibility exists of additional economic losses due to incomplete repairs. To theauthors' knowledge, no

Accepted manuscript doi:
10.1680/jmaen.2018.16

statistical information is available on the occurrences of vessel slippage during crew transfers.

Previously, Josse et al. (2011) presented a mechanical system in which the hydrodynamic forces were ignored and the angle of the vessel against the monopile was the only parameter assumed to affect the frictional contact. However, König et al. (2017) emphasised the necessity of calculating the hydrodynamic forces within the wave field to improve the determination of wave loading on the vessel. This study assumed that hydrodynamic forces have the largest effect on the frictional contact and an approximation for the diffracted wave height as a function of wave length was derived but no attempt was made to extend the calculations to quantify the local water particle kinematics within this region. Edesses 2017 presented a preliminary approach to this difficulty whereby the diffracted wave forces on a surface-piercing circular vertical cylinder and the local water surface elevation field were calculated for linear regular waves with varying diameter-to-wavelength ratios.

Improved approximation of the local irregular wave field will allow for future identification of the limiting conditions under which the total vertical hydrodynamic force on the vessel overcomes the frictional contact force between the vessel's fender and the transition piece on the monopile, thereby causing the vessel to slip. The aim of this study is to present methods to improve the current knowledge of the wave-structure interaction and local wave field relevant to a CTV under operational conditions.

Satisfactory evaluation of wave forces in the vicinity of the turbine monopile is challenging in irregular seas of finite depth, where the influence of the monopile on the local hydrodynamics depends on the monopile diameter-to-wavelength ratio. In shallower seas, nonlinearities in the wave field due to bottom effects can be introduced (Schløer et al., 2011). Determination of the wave forces within this region provides a preliminary step towards resolving the factors affecting CTV motion. Analytical methods exist that approximate the incident wave forces in linear irregular seas, but numerical methods, such as those used in OpenFOAM, allow inclusion of nonlinear terms within the fluid flow equations.

This paper is a companion to Edesess et al. (2017), which describes the calibrated input conditions used herein. Two methods are presented: one analytical and the other numerical, for calculating the local diffracted free surface elevation, the water particle kinematics fields and the wave-induced in-line force on an offshore wind turbine monopile in unidirectional irregular waves. The turbine monopile is idealised as a surface-piercing, bottom-fixed, smooth vertical cylinder of uniform diameter experiencing loading from long-crested, small-amplitude waves. In the CTV-turbine monopile system, it is usual to assume that the transition piece is located leeward of the turbine monopile in order to shelter the CTV from incident waves, as illustrated in Figure 1. It should be noted that Figure 1 does not show the hydrodynamic forces incident on the vessel.
The aim of this paper is to compare analytical and numerical predictions of water particle kinematics and wave loading force spectra, using data made available from a single wave buoy at Teesside Offshore Wind Farm in the southern North Sea (Figure 2) and supplied by EDF Energy Renewables. Teesside Offshore Wind Farm is a typical example of a fully commissioned fixed-monopile offshore wind farm and inclusion of *in-situ* wave data is beneficial for determining authentic wave conditions. The paper has the following objectives:

Accepted manuscript doi:
10.1680/jmaen.2018.16

1. To test the suitability of statistical wave analysis and linear diffraction theory to approximate the free surface elevation, wave particle kinematics, significant wave height and in-line wave force on a fixed monopile wind turbine support structurein a given unidirectional sea state.

2. To apply the input wave conditions produced by the *customSpectrum* boundary condition developed by Edesess et al. (2017) and investigate the use of OpenFOAM to simulate the same sea state and wave loading on an offshore wind turbine monopile.

A better understanding of the water particle kinematics incident on a CTV in a given sea state is invaluable for safe, effective crew transfers and essential in reducing the O & M costs for offshore wind farms. Engineers and small- to medium-enterprises engaged in O & M can benefit from appropriate analytical modelling tools with reduced computational overhead to approximate wave conditions. Additionally, OpenFOAM is a powerful open-source tool for numerically approximating the interaction between ocean waves and a fixed surface-piercing vertical cylinder. It has been estimated that O & M costs could decrease by as much as 35% by 2025 with improvements to the turbine access methods (Taylor et al., 2016). This paper will not extend the calculations for the wave kinematics around the monopile turbine to CTV vessel motion, the intention being to provide a method for creating input sea state conditions that can ultimately provide the hydrodynamic input that can be applied to a vessel motion algorithm, such as a strip theory method.

2. Theory

2.1. Undisturbed linear wave field

The undisturbed wave field is modelled using linear wave theory, see e.g. Dean and Dalrymple (1991), assuming that waves are of small amplitude, the fluid is both incompressible and inviscid, the flow irrotational and possessing a single frequency. The wavelength λ is related to the wave period T through the linear dispersion relation $\omega^2 = gk\tanh kh$, where $\omega = 2\pi / T$ is the wave frequency, $k = 2\pi / \lambda$ is the wave number, h is the water depth and g is acceleration due to gravity. For waves propagating in the x-direction, where the coordinate origin is in the mean water level, the horizontal and vertical water particle velocity components are given respectively as the spatial derivatives of the linear velocity potential ϕ,

$$u = \frac{\partial \phi}{\partial x},\ w = \frac{\partial \phi}{\partial z}, \tag{1}$$

where z is measured vertically upward from the still water level. Similarly the acceleration components are given by

$$\dot{u} = \frac{Du}{Dt},\ \dot{w} = \frac{Dw}{Dt}, \tag{2}$$

where t is time. The free surface elevation of linear, unidirectional, small-amplitude free surface waves is

$$\eta = a\cos\left(kx - \omega t\right), \tag{3}$$

where a is the wave amplitude measured here in m.
Once more invoking the assumption of small-amplitude waves, we represent the local sea state as an irregular wave field composed of the linear superposition of multiple sinusoidal components with varying frequencies, amplitudes and random phases (between 0 and 2π). By superposition, (3) becomes

$$\eta = \sum_{n=1}^{N} a_n \cos\left(k_n x - \omega_n t + \psi_n\right) \tag{4}$$

where a_n is the amplitude, k_n is the wave number, ω_n is the angular frequency and ψ_n is the phase of the n-th wave component. In irregular waves, the linear dispersion relation holds for each frequency of the spectrum, i.e. $\omega_n^2 = gk_n \tanh k_n h$. In a similar manner, the undisturbed horizontal and vertical water particle velocity components in irregular waves may be expressed as

$$u = \sum_{n=1}^{N} a_n \omega_n \frac{\cosh k_n\left(z+h\right)}{\cosh k_n h} \cos\left(k_n x - \omega_n t + \psi_n\right), \tag{5}$$

$$w = \sum_{n=1}^{N} a_n \omega_n \frac{\sinh k_n\left(z+h\right)}{\cosh k_n h} \sin\left(k_n x - \omega_n t + \psi_n\right). \tag{6}$$

A statistical representation of the sea state may be determined by taking a Fast Fourier Transform (FFT) of the free surface displacement to obtain the wave energy spectrum $S_\eta\left(f\right)$ (see e.g. Sumer and Fredsøe (2006)), from which the wave component amplitudes are calculated as

$$a_n = \sqrt{2S_\eta\left(f_n\right)\Delta f}, \tag{7}$$

where Δf is the frequency bin size and f $(=\omega/2\pi)$ is in Hz. The new frequency-dependent system can be verified as representative of the correct sea state by comparing the total energy within the system m_0, to the variance of the original free surface displacement σ_η^2 (Papoulis, 1991; Sumer and Fredsøe, 2006) via

$$m_0 = \int_0^\infty S_\eta\left(f\right) df = \sigma_\eta^2. \tag{8}$$

Henceforth, the spectral dependence on the frequency f will be assumed. The significant wave height H_s is an important statistical parameter that can be obtained from

$$H_s = 4\sqrt{m_0}. \tag{9}$$

The incident water particle velocity components can then be computed from (5) and (6). Further verification that the calculated sea state correctly corresponds to the original data and spectrum can be completed by calculating the spectral function of the new irregular surface elevation, obtained using (4) and equating the variance to that of the original data with (8) (Edesess et al., 2017).

Accepted manuscript doi:
10.1680/jmaen.2018.16

The above analysis applies solely to a unidirectional sea state, which may not represent the bimodal spectra, which might contain additional directional components . Without including directionality in the wave spectrum, the wave particle velocities and free-surface profiles may be overestimated or underestimated. However, to take the wave direction into account in the statistical analysis, wave displacement data taken during identical time intervals at multiple points would be necessary. In this study, as is commonly the case in offshore analysis, data from only one point was available. It is a very complicated task to resolve the prevailing wind-wave-swell directions from a single point (McAllister et al., 2017; Adcock and Taylor, 2009) and so directionality is not included in the present study.

2.2. Wave Forces

The turbine monopile is idealised as a smooth, surface-piercing, fixed circular cylinder of uniform cross-section, with the transition piece neglected in the hydrodynamic study. Assuming linear waves and a wave height-to-water depth ratio < 0.1 for allwaves, the fluid far away from the cylinder is described by linear wave theory and a velocity potential ϕ, as introduced in Section 2.1, may be employed.

Close to the cylinder, viscous surface effects influence the flow field. The local hydrodynamic regime depends on the ambient wave parameters, water depth and length scale of the cylinder. For small diameter cylinders, where $D/\lambda < 0.2$ and D is the diameter of the cylinder, it may be assumed that the presence of the monopile has negligible effect on the pressure field in the passing flow and viscous forces dominate (MacCamy and Fuchs, 1954). As the cylinder diameter-to-wavelength ratio increases, the presence of the cylinder modifies the local hydrodynamic pressure gradient and the inertia force increases, related to wave diffraction. In the drag-inertia regime, both viscous and inertia force components contribute to the loading, and the flow can experience additional influences due to wave nonlinearity or the presence of high-frequency diffracted waves (Swan and Sheikh, 2014). These are additional factors acknowledged but will not be addressed here; an assumption of linearity will be made throughout. The Reynolds number (Re) and Keulegan-Carpenter number (KC) are commonly used to describe the ratio of inertia-to-viscous forces and the ratio of drag-to-inertia forces respectively, for any given fluid flow past an obstacle (Sarpkaya and Isaacson, 1981). These are given by

$$Re = \frac{U_0 D}{\nu}, \tag{10}$$

$$KC = \frac{T U_0}{D}, \tag{11}$$

where U_0 is the magnitude of the incident velocity vector and ν is the coefficient of fluid kinematic viscosity (Faltinsen, 1990). At the site of interest, Teesside Offshore Wind Farm, a typical monopile is of diameter $D \approx 5$ m, and the corresponding Reynolds number and Keulegan-Carpenter number ranges are $1.2\times10^6 < Re < 3.6\times10^6$ and $0.35 < KC < 1.1$. In this regime, the KC number remains small across the range of wave periods T, implying that the inertia forces are large. Whilst it might be expected that vortices form in this Reynolds number range (Zdravkovich, 1997), vortex shedding does not occur when $KC < 3$ (Sarpkaya, 2006). At high Re and low KC, a third non-dimensional parameter, $\beta = Re/KC$ can be

Accepted manuscript doi:
10.1680/jmaen.2018.16

used in addition to indicate viscous forces present in the flow (Chaplin, 2000; Johanning et al., 2001; Sarpkaya, 2006) and is given by

$$\beta = \frac{fD^2}{\nu} \tag{12}$$

for the wave frequency f measured in Hz.

Two methods are presented herein for evaluating the wave-induced force on the monopile, depending on the cylinder diameter-to-wavelength ratio: one for small-diameter cylinders, the other for larger-diameter cylinders.

2.2.1. Wave Force on a Small Diameter Cylinder

The Morison equation (Morison et al., 1950) is commonly used to estimate the total in-line force on a small-diameter cylinder in linear and non-linear flow. It comprises the linear sum of drag and inertial force components and is evaluated using the water particle velocity and acceleration calculated in the absence of the cylinder. By integrating over the submerged length of a vertical surface-piercing cylinder (that extends from the bed to above the free surface), the total in-line force exerted on a cylinder is given by

$$F_M = \frac{1}{2} C_d D \rho \int_{z=-h}^{z=\eta} |u| u dz + \rho C_m \frac{\pi D^2}{4} \int_{z=-h}^{z=\eta} \dot{u} dz \tag{13}$$

where ρ is the fluid density, u is the in-line velocity component calculated from (5), and $\dot{u}$ is the in-line acceleration component from (2). The drag and inertia coefficients, C_d and C_m respectively, are usually obtained experimentally but for high β values they can be calculated from

$$C_d = \frac{3\pi^3}{2KC}\left[(\pi\beta)^{-1/2} + (\pi\beta)^{-1} - \frac{1}{4}(\pi\beta)^{-3/2} \right], \tag{14}$$

and

$$C_m = 2 + 4(\pi\beta)^{-1/2} + (\pi\beta)^{-3/2}, \tag{15}$$

as shown by Wang (1968).

2.2.2. Wave Force on a Large Diameter Cylinder

Linear diffraction theory applies to an inertia-dominated wave flow past a large-diameter monopile when the ratio of diameter-to-wavelength $D\lambda \geq 0.2$. The analytical solution for the total diffracted linear velocity potential ϕ_D was presented for monochromatic waves by MacCamy and Fuchs (1954) to be

$$\phi_D = -i\frac{ga}{\omega}\frac{\cosh k(z+h)}{\cosh kh} \cdot \sum_{m=0}^{\infty} \epsilon_m i^m \left[J_m(kr) - H_m^{(1)}(kr) \frac{J_m'(kR)}{H^{(1)'}(kR)} \right] \cos m\theta e^{-i\omega t} \tag{16}$$

Accepted manuscript doi:
10.1680/jmaen.2018.16

where i = $\sqrt{-1}$, J_m is the Bessel function of the first kind of order m, ϵ_0 = 1 and ϵ_m = 2 for all $m>0$, $H_m^{(1)}$ is the Hankel function of the first kind of order m and a prime indicates a derivative. On the cylinder wall, the radial distance from the centre of the column is $r=R$, where R is the cylinder radius. The angle θ is measured positive in an anticlockwise direction from the x-axis in a horizontal plane, giving $x=r\cos\theta$. The time-dependent diffracted surface elevation η_D is found from the linearised Bernoulli equation, as in Sumer and Fredsøe (2006),

$$\eta_{D}=-\frac{1}{g}\frac{\partial\phi_D}{\partial t}. \quad (17)$$

Conventional diffraction analysis assumes regular monochromatic waves and can overestimate wave heights in the vicinity of an obstacle, as discussed by Goda (1985). The diffracted wave height in a polychromatic wave field is derived from the superpositionof the diffracted wave solution obtained for each individual wave component, where the frequencies of radially outward moving diffracted waves correspond to frequencies of incident waves (Swan and Sheikh, 2014). Linear superposition, based upon (4), allows the irregular diffraction solution to be expressed as

$$\eta_D = Re\{\sum_{n=1}^{N} a_n e^{-i\omega t+\psi_n}\cdot[\sum_{m=0}^{M}\epsilon_m (i)^m \cdot\left(J_m\left(k_n r\right)-H_m^{(1)}\left(k_n r\right)\frac{J_m^{'}\left(k_n R\right)}{H_m^{(1)'}\left(k_n R\right)}\right)\cos m\theta]\}. \quad (18)$$

It should be noted that (18) is only valid within the linear regime and does not hold when nonlinear diffraction becomes significant. Whilst the linear formulation provides a useful approximation for diffraction in small, non-breaking waves, the inherent nonlinearity existing within the sea suggests that inclusion of second-order diffraction terms would better represent the ocean waves diffracted by a monopile Kriebel (1990); Yang and Ertekin (1991). However, correct inclusion of second-order terms is debated and is beyond the scope of the present analysis.

Following the steps outlined in Section 1, the diffracted surface elevation spectrum $S_{\eta,D}$ is first evaluated, with (7) implemented to calculate the individual diffracted amplitudes from the diffracted spectrum. The diffracted water particle kinematics, u_D and w_D in (5) and (6), are then determined.

The total wave force on a large-diameter cylinder can be determined from linear diffraction theory by integrating the surface pressure over the wetted surface of the cylinder. The pressure field is obtained from the unsteady Bernoulli equation and the resulting in-line diffracted force is obtained by extending the single-frequency potential of MacCamy and Fuchs (1954), given by (7), to include all frequencies included in (4),

$$F_{D}=2\rho g\sum_{n=1}^{N}\frac{a_n}{k_n}\frac{\cosh k_n(h+z)}{\cosh k_n h}\cdot G_n(k_n R)\cos(w_n t-\beta_n-\psi_n) \quad (19)$$

where

$$G_n\left(k_n R\right)=\frac{1}{\sqrt{J_1^{'}(k_n R)^2+Y_1^{'}(k_n R)^2}} \quad \text{and} \quad \tan\beta_n=\frac{J_1^{'}\left(k_n R\right)}{Y_1^{'}\left(k_n R\right)} \quad (20)$$

Accepted manuscript doi:
10.1680/jmaen.2018.16

in which Y_1 is the Bessel function of the second kind of order 1, and all other values remain as above.

3. Numerical Model

The open-source C++ library of fluid solvers, OpenFOAM version 2.4.0, is employed to model the wave field numerically in the vicinity of the cylinder. The numerical model is based on the continuity and Navier-Stokes momentum equations for unsteady motion of an incompressible, viscous fluid. Numerical predictions are then compared to the analytical solutions outlined in Section 2.1.
Multiphase fluid flow at the air-to-water interface is modelled using the volume of fluid (VOF) method. VOF is based on the Marker and Cell (MAC) method which calculates the volume fraction of fluid-to-air present within each cell and then uses a single averaged value across the whole cell (Hirt and Nichols, 1981).

The present simulations are produced using a modification of the multiphase solver *interFoam* devised by Jacobsen et al. (2011) that facilitates wave generation and absorption. The modification, called *waves2Foam*, uses the VOF method coupled with the Reynolds-Averaged Navier-Stokes (RANS) formulation to generate the free surface flow.

Wave types available in the *waves2Foam* release include linear waves (Stokes 1st order), nonlinear (Stokes 2nd order, Stokes 5th order and cnoidal) waves, and irregular waves from either a JONSWAP or Pierson-Moskowitz spectrum. Edesess et al. (2017) presented a further boundary condition, *customSpectrum*, that can be used with the *waveFoam* solver to produce open boundary input data as a free surface elevation time series derived from observed wave spectra S_η. Calibration of the *customSpectrum* boundary condition is described by Edesess et al. (2017).

3.1. Mesh parameters from sea state values

The computational mesh was created using the open-source meshing software, GMSH. Figure 3 depicts the computational domain and mesh structure. The magnified inset shows where the cells are refined in the transition zone and within the wake of the cylinder.
Previous mesh convergence studies conducted for linear waves in the vicinity of a monopile by Edesess 2017, and for irregular waves in the open sea by Edesess et al. (2017), showed that a minimum of 75 cells per modal wave length in the horizontal direction and 7 cells per wave height in the vertical direction were sufficient to reproduce the correct sea state.

Relaxation zones of length λ_m, where λ_m represents the modal wavelength, are applied at the inlet and outlet of the computational domain to absorb outgoing and reflected waves.

A full description of the implementation of the numerical model in OpenFOAM, using the VOF method and wave generation and absorption with *waveFoam* is provided as an Appendix.

Accepted manuscript doi:
10.1680/jmaen.2018.16

4. Results and Discussion

We now compare analytical and numerical predictions of the wave particle kinematics in the vicinity of a turbine monopile. A validation case for a linear wave is presented first. Following validation, four sets of data were considered from separate 24-hour periods, each pertaining to a different season of the 2015/2016 year (wave buoy data provided by the Operations Team at EDF Energy Renewables). The datasets constitute free surface displacement time series measured by a single Datawell Waverider DWR-MkIII wave buoy located at Teesside Offshore Wind Farm in the southern North Sea off the east coast of the United Kingdom, as in Figure 2.

4.1. Validation of numerical model for regular waves

The OpenFOAM model is validated by simulating a linear regular wave of period T = 8 s, height H = 1.0 m, water depth h = 15 m and monopile diameter D = 5 m, where the depth and diameter values are selected based on typical values found at Teesside Offshore Wind Farm. This corresponds to a wavelength λ of 82 m. The water depth and monopile diameter are kept constant throughout all regular and irregular wave simulations. The computational domain has horizontal length $x = 4\lambda$, width $y = 1.5\lambda$ and extends from the bed to 10 m above the free surface in the vertical z direction to avoid surface diffusion.

An inlet-outlet boundary condition, which switches between zero-gradient for fluid flowing out of the domain and fixed-value for fluid flowing into the domain, is applied at the atmospheric upper boundary of the domain. Both slip and no-slip boundary conditions on the cylinder are considered for comparative purposes. The slip boundary condition matches the assumptions underpinning (18), where inertial effects dominate over viscous. A no-slip boundary condition, valid for smaller diameter-to-wavelength ratios, effectively includes the effect of viscosity on the near-wall boundary layer. Boundary conditions at the sea bed are the same as applied on the cylinder wall and a fixed-value wave absorption boundary condition at the outlet.

A mesh convergence analysis was undertaken for the linear verification model, where both models used a vertical cell height of Δz = 0.125 m. Mesh 1 used a minimum Δx = 0.565 m and mesh 2 used a minimum Δx = 0.368 m, within the transition zone near the cylinder. Outside the transition zone, mesh 1 used 75 cells per wavelength and mesh 2 used 105 cells per wavelength. A slip boundary condition was applied at the cylinder wall throughout. Each simulation was run in parallel across 24 processors using a supercomputer at the Irish Centre for High-End Computing.

4.1.1. Results from numerical model validation

Excellent agreement between the analytical and numerical predictions was achieved using mesh 1. Figure 4 presents comparisons between the numerical predictions and analytical solutions from linear wave theory and linear diffraction theory for the surface elevation. The surface elevation values are calculated at the point corresponding to the location $(x, y) = (0, R)$ where R is the radius of the cylinder.

Accepted manuscript doi:
10.1680/jmaen.2018.16

Diffraction effects should be minimal for the wave period in this verification case, which is seen in the figures as the solutions differ minimally between an undisturbed surface elevation, the diffracted surface elevations, and numerical predicted surface elevations.
Figure 5 presents a comparison of the wave forces corresponding to the wave field in Figure 4. The numerical predictions of wave forces for both meshes correspond well to the calculation of wave force using both the Morison equation and the MacCamy & Fuchs diffraction solution. The similarity between values obtained through all methods implies that viscous forces contribute minimally to the total force for the given wave period.

4.2. Simulation of irregular seas

Table 1 lists minimum and maximum values of wave period T, T_{min} and T_{max}, considered in the sea state simulations, together with the peak energy values and the significant wave height for each data set. The total CPU hoursrequired for each OpenFOAM simulation are also listed. Minimum and maximum wave periods were determined by interpreting the input wave spectrum (Edesess et al., 2017).

For those sea states containing additional spectral peaks at higher frequency values and shown in bimodal spectra, such as occurred in December 2015, it was necessary to include waves with period as short as $T = 2$ s (and corresponding wavelength $\lambda \leq 6$ m) in the simulations. The computational cost was controlled by using a minimum of only 7 cells per wavelength for the highest frequencies, ensuring that the modal wave length was properly sampled whilst limiting the overall number of cells. The associated risk here is that the high-frequency waves could be under-sampled during the wave generation process, lowering overall accuracy and losing information at these frequencies. It should be noted that the same method was utilised by Edesess et al. (2017) who found that inaccuracies in the inlet wave field were minimal in comparison to the savings in computational time. Each simulation was run for t^* = 40, where $t^* = t / T_p$ in which T_p is the modal wave period.

4.2.1. Numerical visualisation of wave free surface

Figure 6 presents a visualization of the wave free surface at time $t^* = 35$ for the sea state for March 2016, obtained using the numerical model with a surface-piercing, circular cylinder representing a turbine support column. The values of surface Reynolds number, Keulegan-Carpenter number and β are 1.22 x 10^6, 0.35 and 3.49x 10^6 respectively. A diffraction pattern is visible upstream from the wave-wave interaction of the incident waves waves reflected from the monopile whereas a laminar wake has developed downstream. Viscous effects cause a velocity reduction in the wake of the monopile. There is evidence of vorticity streaming into the wake but no vortex shedding, which is to be expected at such a low Keulegan-Carpenter number. Similar diffraction-wake patterns were obtained using the numerical model for input wave data from each season.

4.2.2. Spectral analysis of wave field

Figure 7 presents wave spectra obtained by taking the Fourier transform of the free surface elevation time series at the rear stagnation point of the monopile cylinder for each of the four seasons. Data are obtained from September 2015, December 2015, March 2016, and‘ boat landing, placed with respect to tidal movement and typical wave direction. The boat landing

is located downstream of the turbine monopile in unidirectional waves. It is commonly believed that this arrangement allows the monopile to block the CTV from directly oncoming or beam waves.

Each subplot shows the undisturbed wave spectrum S_η, the diffracted wave spectrum obtained using linear diffraction theory $S_{\eta,\mathrm{D}}$, the numerical wave spectrum using a slip-boundary condition on the cylinder $S_{\eta,\mathrm{S}}$, and the corresponding wave spectrum using a no-slip condition $S_{\eta,\mathrm{N}}$. The undisturbed wave spectral estimates were previously validated against raw *in situ* sea state data by Edesess et al. (2017). The importance of diffraction is evident in the decrease in surface elevation visible in the numerical predictions and analytical diffraction solution.

For the bimodal winter data set, the numerical predictions do not appear to retain the second peak at about f = 0.4 Hz ($T_p \sim 7$ s), apparent in the undisturbed wave field and diffraction solution. However, a decrease in energy of high-frequency waves is also visible in the diffraction solution, indicating that lower-frequency waves contain greater energy, which is also captured by the numerical predictions. The summer dataset also contains a second peak in the undisturbed formulation, although the high-frequency components contribute minimally to the total energy. The second peak is greatly diminished in the analytical diffraction solution and disappears in the numerical predictions.

The analytical diffracted wave spectrum in Figure 7 showed a reduction from the incident wave spectrum, in broad agreement with Goda (1985), who found that an irregular wave diffraction solution may have a lower diffracted wave height thanmight be expected from a regular diffraction solution. Both numerical results using slip and no-slip boundary conditions exhibited this reduction in wave height around the monopile, compared to the undisturbed wave elevation spectrum. Better agreement was achieved between the results from the analytical diffraction formulation and the numerical simulation using a slip boundary condition. This result is expected because both methods neglect viscous wall effects. Axes values in all figures were chosen to better represent the results of each seasonal spectra below.
Table 2 lists values of significant wave height H_s determined from the undisturbed and diffracted wave fields. The significant wave height obtained for the case with a monopile present was substantially lower than that in the undisturbed wave field in all models.

The discrepancy between the analytical and numerical predictions of diffracted significant wave height ranges from 6.3% for March 2016 data set to 23.8% for the December 2015 dataset.
Extensive efforts were made to capture the high-frequency second peak in the winter data set by improving the mesh resolution. In the first attempt, the cell length in the wave direction was divided in half to allow the shortest waves within the spectrum to be sampled using a minimum of 14 cells per wave. This mesh resolution also meant that the longest waves now contained approximately 180 cells in the wave direction and significantly increased the computational overhead but showed negligible improvementin the results.

Accepted manuscript doi:
10.1680/jmaen.2018.16

A further attempt was made, in which the cells at the free surface were refined to ensure at least 12 cells at the free surface. The significant wave height in this data set is lower than for the other three seasons. This reduction in wave height means that it can be difficult to sample properly the cells at the free surface whilst maintaining an acceptable aspect ratio and reducing the computational overhead. In order to ensure the refined mesh quality remains acceptable, which can be checked with the *checkMesh* utility included with OpenFOAM, it was also necessary to increase the number of cells both in the wave (x) direction and the transverse (y) direction. This increased CPU time significantly but the results were again unsatisfactory andthe poorer mesh aspect ratio was likely to have introduced additional numerical errors. It is recommended that the numerical model of the winter sea state is explored more in the future, given that a final determination on the suitability of OpenFOAM for capturing bimodal spectra has not been demonstrated here.

Analytical values for the water particle velocity components were calculated from the undisturbed wave spectrum S_η and the diffracted wave spectrum $S_{\eta,\mathrm{D}}$. Numerical estimates of the diffracted water particle velocities were also obtained from the numerical model. Figure 8 presents the horizontal and vertical water particle velocity component spectra obtained over the four seasons. It is apparent from the laminar wake shown in Figure 6 that the horizontal velocity values in the near-wake are minimal. Velocity values in Figure 8 are obtained again at $(x, y) = (0, R)$. Vertical velocity contributions $\mathrm{S_w}$ are more apparent within the wake.

The CPU run times, listed in Table 1, are unreasonable for practical design where engineers might require knowledge of current sea state conditions in order to make swift maintenance decisions. For this reason, it is desirable to improve the analytical model in the future to incorporate nonlinear viscous terms for sea state approximations without relying on the impractical run times required by the OpenFOAM model.

4.2.3. Spectral analysis of wave loading

We now consider the forces acting on the idealised column. Table 3 lists the seasonal values of Keulegan-Carpenter number KC, frequency parameter β, and drag and inertia coefficients C_d and C_m. For all data sets, C_d and C_m have been calculated using the method proposed by Wang (1968). Table 4 lists the peak force on the monopile for each season using the different force calculation methods outlined in Section 2.2 Values of C_d and C_m listed in the table were utilised in the in-line force calculation using the Morison equation. The subscript M relates to the force estimate based on the Morison equation (13), subscript D denotes the estimate based on linear diffraction theory (19) and subscripts S and N refer to forces calculated through integration of the total surface pressure obtained numerically using slip and no-slip cylinder wall boundary conditions, respectively.

The C_d and C_m coefficients vary little across the seasons with a slight increase in C_d seen in the winter data set. The low value of C_d shows that the drag term in the Morison equation provided a small contribution to the total force. This implies that diffraction theory is acceptable at providing force estimates for a typical large-diameter monopile in the southern North Sea. However, it should be noted that linear diffraction theory omits the influence of higher-order wave pressure, which is proportional to the square of the wave height, on the

Accepted manuscript doi:
10.1680/jmaen.2018.16

analytical wave force. A second-order diffraction method, such as that introduced by Chau and Eatock Taylor (1992), might improve the analytical model for a wider range of sea states.

Figure 9 shows the force spectra obtained for each of the seasons. In all cases, the spectral values obtained using CFD with a no-slip condition have smaller amplitude than the other predictions. The Morison spectra gave the highest predictions, with a pronounced second peak occurring in the winter. The closest agreement is between the spectra obtained using analytical diffraction theory and CFD with a slip condition.

No experimental results were available for use in this work. Experiments with irregular waves interacting with a monopile in a wave flume, similar to those conducted by Nielsen et al. (2012) or Chella et al. (2012), could be used to further verify the numerical and analytical predictions.

4.3. Discussion

In all the wave, velocity, and force spectra considered, the modal wave period remained nearly constant throughout the year, except for the bimodal sea state in December 2015 and June 2016, where an modal wave period was apparent from the second peak. The OpenFOAM numerical spectra agree well with their analytical counterparts for the unimodal sea states found in September 2015 and March 2016. Although the summer dataset also has a small second peak, the contribution to the total energy within this peak is minimal and satisfactory agreement is also achieved for June 2016. The comparisons match less well in December 2015 (where the higher frequency force components are not apparent in the numerical spectra, unlike the analytical spectrum).

Numerical predictions obtained using slip and no-slip boundary conditions are generally similar over the range of cases considered, indicating that the linear diffraction effects were small. Nevertheless, current trends to reduce the costs of energy produced by offshore wind turbines have led to an increase in the diameter of the turbine monopile, corresponding to a more inertia-dominated flow and an increased importance on improving diffraction models to incorporate the high-frequency diffracted waves.

Despite the extensive run time required by OpenFOAM, the numerical model is effective for visualisation of the free surface flow around the cylinder where viscous effects and complexities within the fluid flow can be considered for a more complete model than that presently provided by the analytical method. Moreover, the benefit of the open-source structure of OpenFOAM allows the wave conditions at Teesside Offshore Wind Farm to be approximated numerically, rather than relying solely on experimental or approximating values.

5. Conclusions

This paper has investigated the use of linear diffraction theory and computational fluid dynamics (CFD) for determining the free surface elevation η, significant wave height H_s, and water particle velocity components u and w close to a surface-piercing vertical cylinder representative of an offshore wind turbine monopile situated in the southern North Sea.

Accepted manuscript doi:
10.1680/jmaen.2018.16

The total in-line force in unidirectional waves on the monopile has also been determined. Linear diffraction theory is fast to implement, but neglects nonlinearity and viscous effects. For non-breaking waves of small-amplitude, linear diffraction can provide a suitable estimate of the diffracted wave height and kinematics for larger wavelength-to-diameter ratios, although linear diffraction has been found to underestimate the maximum wave run-up by up to 50% when nonlinearity is consequential Kriebel (1990). The CFD model is based on OpenFOAM and is expensive in terms of computational resources, but resolves nonlinear and viscous effects. OpenFOAM was run using a constant value of kinematic fluid viscosity, which meant that the fluid was considered laminar. In all cases considered, it was found that the predictions from the numerical model were not affected greatly by the choice of slip or no-slip cylinder wall boundary condition.

Comparison tests were undertaken using observed sea states for all four seasons at Teesside Offshore Wind Farm in 2016. Close agreement was obtained between the linear diffraction theory and OpenFOAM estimates of wave, water particle velocity component, and force spectra for three of the datasets. The results were in relatively poor agreement for the winter dataset corresponding to a bimodal wave distribution, although the loss of the second peak in the numerical prediction does correspond to a reduction in energy within the second peak also apparent in the diffraction formulation.

It is recommended that additional improvements to the model be made in the future to investigate the use of a spreading function or an appropriate mechanism to reproduce multidirectional sea states, and crossing seas, both of which could result in bimodal spectra. It is also recommended that a higher-order diffraction method should be pursued to predict the effect of wave nonlinearity, which is important when considering transfer vessel motions in the vicinity of the monopile. It should be noted that although OpenFOAM is a fully nonlinear model, its accuracy is limited by the lack of turbulence component in these model simulations. However, the low KC number expected for all sea state conditions suggests the dominance of inertia forces, justifying the exclusion of turbulence model. Even so, this relatively efficient approach provides sufficient physics for later CTV motion analysis to take place.

Acknowledgements

The authors are grateful to the Operations Team at EDF Energy Renewables Teesside Offshore Wind Farm for access to *in situ* wave buoy data. The authors are also grateful to Dr. Tariq Dawood for his advice concerning the Teesside wind farm site andto Alexis Billet of Resilience Energy Ltd., who helped design the research project and partly funded its initial stages. This research was supported by the SFI Centre for Marine and Renewable Energy Ireland (MaREI) and EDF Energy.

Appendix

A. Numerical Model

The numerical model applied in OpenFOAM version 2.4.0 is based on the continuity and Navier-Stokes momentum equations for unsteady motion of an incompressible, viscous fluid,

Accepted manuscript doi:
10.1680/jmaen.2018.16

$$\nabla \cdot \boldsymbol{u} = 0 \tag{21}$$

and

$$\frac{\partial}{\partial t}\boldsymbol{u} + (\boldsymbol{u} \cdot \nabla)\boldsymbol{u} = -\nabla p + \mu \nabla^2 \boldsymbol{u} + F_{\boldsymbol{B}}, \tag{22}$$

where $\boldsymbol{u}$ is the velocity vector, p is the hydrodynamic pressure in excess of hydrostatic, μ is the coefficient of fluid kinematic viscosity, and $F_{\boldsymbol{B}}$ is an external source term, which relates solely to gravitational acceleration in the vertical direction herein.

The volume of fluid (VOF) method uses a volume fraction function α, defined as the averaged flux value, obtained numerically from the solution of the following transient advection equation

$$\frac{\partial \alpha}{\partial t} + \nabla \cdot [\boldsymbol{u}\alpha] + \nabla \cdot [u_r \alpha (1-\alpha)] = 0, \tag{23}$$

where α takes the values

$$\alpha = \begin{cases} 0, & \text{air} \\ 1, & \text{water} \\ 0 \le \alpha \le 1, & \text{interface}. \end{cases}$$

The term $\boldsymbol{u}_r$ in (23) refers to the relative velocity (Jacobsen et al., 2011). The final term on the left-hand-side of (23) is an artificial compression term necessary to reduce interfacial smearing. The volume fraction function can then be multiplied by any specific property such as velocity (**u**) or pressure (p) to determine the average value of that property within each cell. OpenFOAM uses the finite volume method (FVM) to discretise equations (21), (22) and (23), which then form an algebraic system of equations.
Time integration is carried out using the Euler explicit method and numerical stability is achieved through an automatically adjustable time-step size Δt determined by the Courant criterion,

$$\mathrm{Co} = \frac{\Delta t |\boldsymbol{u}|}{\Delta x} \le 1, \tag{24}$$

where Δx is the cell size and $\boldsymbol{u}$ is the fluid velocity (Courant et al., 1967).

A.1. Wave Absorption

A challenge for simulating numerically open sea conditions is the need to minimise the length of the computational domain, CPU time, and risk of contamination from reflected waves reaching the open boundary. Wave reflection is avoided here through the useof relaxation zones (included in *waves2Foam*). Relaxation zones act as numerical sponge layers to absorb any outgoing or reflected waves. These are applied at the inlet (to absorb upstream-travelling wave components reflected from the cylinder) and at the outlet (to absorb outgoing waves). In *waves2Foam*, the relaxation zones are defined by the following relaxation function

Accepted manuscript doi:
10.1680/jmaen.2018.16

$$\alpha_R(\chi_R) = 1 - \frac{exp(\chi_R^\gamma) - 1}{exp(1) - 1} \text{ for } \chi_R \in [0,1], \tag{25}$$

where χ_R is a spatial tracker that is set equal to 0 at the start of the relaxation zone and 1 at the end, with γ being a relaxation coefficient. Within the relaxation zone, the wave is absorbed using the function

$$q = \alpha_R q_{computed} + (1 - \alpha_R) q_{target}, \tag{26}$$

in which q is either the fluid volume fraction α or the velocity $\boldsymbol{u}$, where $\boldsymbol{u}_{target} = 0$. Relaxation zones are usually recommended to have length of at least 1.5λ (Chen et al., 2014) but the length of the relaxation zones can be adjusted by altering the value of γ in (25). Edesess et al. (2017) found that the length of the relaxation zones can be reduced to λ_m while still eliminating reflection, where λ_m is the wavelength corresponding to the modal period when a value of $\gamma = 1$ was used in equation (25).

Nomenclature

m_0 Zeroth moment, m
$S_\eta(f)$ Frequency spectrum of surface elevation, m^2/Hz
σ_η^2 Variance of free surface elevation, m^2
H_s Significant wave height, m
n Number of frequency components
a_n Amplitude Components, m
df Frequency step size (Hz)
η Location of free surface, m
u Horizontal velocity component, m/s
w Vertical velocity component, m/s
$\dot{u}$ Horizontal Acceleration Component, m/s^2
$\dot{w}$ Vertical Acceleration Component, m/s^2
k_n n-th component wave number, rad/m
ω_n Angular wave frequency components, rad/Hz
z Location measured vertically upwards from mean water level, m
x Horizontal Location, m
ψ_n Random phase values in the range $0 \le \psi \le 2\pi$
h Mean water depth, m
g Vertical acceleration due to gravity, m/s^2
$\boldsymbol{u}$ Velocity vector, ms
p^* Pressure in excess of hydrostatic, kg/m^3
τ Reynolds stress tensor
Γ_T Surface tension coefficient

α Volume of fluid fraction
μ Relaxation zone coefficient value
T_p Modal period, s
Co Courant number
F_D Diffracted force, N
$G(kR)$ Diffraction solution parameter
$S_{F,D}$ Diffracted force spectrum, N^2 Hz
$S_{F,M}$ Morison force spectrum, N^2 Hz
$H_{s,D}$ Diffracted significant wave height, m
λ_p Modal wavelength, m

Accepted manuscript doi:
10.1680/jmaen.2018.16

REFERENCES

Adcock TAA and Taylor PH (2009) Estimating ocean wave directional spreading from an Eulerian surface elevation time history. *Proceedings of the Royal Society A* **465**: 30833102.

Breton SP and Moe G (2009) Status, plans and technologies for offshore wind turbines in Europe and North America. *Renewable Energy* **34(3)**: 646–654.

Chaplin JR (2000) Hydrodynamic damping of a cylinder at $\beta \approx 10^6$. *Journal of Fluids and Structures* **14**: 1101–1117, doi:10.1006/jfls.2000.0318.

Chau FP and Eatock Taylor R (1992) Second-order wave diffraction by a vertical cylinder. *Journal of Fluid Mechanics* **240**: 571–599.

Chella MA, Tørum A and Myrhaug D (2012) An overview of wave impact forces on offshore wind turbine substructures. In: Procedia, E.(Ed.), *Technoport RERC Research 2012* (Procedia E, ed.), pp. 217–226.

Chen L, Zang J, Hillis AJ, Morgan GCJ and Plummer AR (2014) Numerical investigation of wave-structure interaction using OpenFOAM. *Ocean Engineering* **88**: 91–109.

Corbetta G, Pineda I and Moccia J (2014) *The European offshore wind industry - key trends and statistics 2013*. *Tech rep.*, European Wind Energy Association, Brussels, Belgium.

Courant R, Friedrichs K and Lewy H (1967) On the partial difference equations of mathematical physics. *IBM Journal of Research and Development* **11(2)**: 215–234.

Dalgic Y, Lazakis I and Turan O (2015a) Investigation of optimum crew transfer vessel fleet for offshore wind farm maintenance operations. *Wind Engineering* **39(1)**: 31–52.

Dalgic Y, Lazkis I, Dinwoodie I, McMillan D and Revie M (2015b) Advanced logistics planning for offshore wind farm operation and maintenance activities. *Ocean Engineering* **101**: 211–226.

Dean RG and Dalrymple RA (1991) *Water Wave Mechanics for Engineers and Scientists*, vol. 2. World Scientific Publishing Co. Pte. Ltd., Covent Garden, London WC2H 9HE.

Edesess AJ, Kelliher D, Borthwick AGL and Thomas GP May 2017 Improving global accessibility to offshore wind power through decreased operations and maintenance costs: a hydrodynamic analysis. In *Energy Procedia*, Springer.
Faltinsen OM (1990) *Sea Loads on Ships and Offshore Structures*. Cambridge University Press.

Goda Y (1985) *Random Seas and Design of Maritime Structures*. The University of Tokyo Press, Tokyo, Japan.

Hirt CW and Nichols BD (1981) Volume of Fluid (VOF) method for the dynamics of free boundaries. *Journal of Computational Physics* **39**: 201–225.

Hoffman M (2011) A review of decision support models for offshore wind farms with an emphasis on operation and maintenance strategies. *Wind Energy* **35(1)**: 1–16.

IEA (2013) *Technology Roadmap - Wind Energy*. *Tech. rep.*, International Energy Agency (IEA), Paris.

IRENA (2016) *Wind power technology Brief E07*. *Technology brief*, Energy Technology Network - Energy Technology Systems Analysis Programme (IEA - ETSAP) and International Renewable Energy Agency (IRENA).

Jacobsen NG, Fuhrman DR and Fredsøe J (2011) A wave generation toolbox for the open-source CFD library: OpenFOAM. *International Journal for Numerical Methods in Fluids* **70**: 1073–1088.

Johanning L, Bearman P and Graham J (2001) Hydrodynamic damping of a large scale surface piercing circular cylinder in planar oscillatory motion. *Journal of Fluids and Structures* **15**: 891–908.

Josse T, Billet A and Leen SB (2011) Prediction of supply vessel motion during transfer to a fixed structure. In *Proceedings of the 30th International Conference on Ocean, Offshore and Arctic Engineering*.

König M, González DF, Abdel-Maksoud M and Düster A (2017) Numerical investigation of the landing manoeuvre of a crew transfer vessel to an offshore wind turbine. *Ships and Offshore Structures* **12(sup1)**: S115–S133. URL http: //dx.doi.org/10.1080/17445302.2016.1265883

Kostecki S (2014) Random vortex method in numerical analysis of 2d flow around circular cylinder. *Studia Geotechnica et Mechanica* **36**: 57–63.

Kriebel DL (1990) Nonlinear wave interaction with a vertical circular cylinder. part i: Diffraction theory. *Ocean Engineering* **17(4)**: 345–377.

MacCamy RC and Fuchs RA (1954) *Wave forces on piles: a diffraction theory*. *Tech. Rep. 69*, U.S. Army Beach Erosion Board Technical Memo.

Maples B, Saur G, Hand M, van der Pieterman R and Obdam T (2013) *Installation, Operation, and Maintenance Strategies to Reduce the Cost of Offshore Wind Energy*. *Technical report*, National Renewable Energy Laboratory (NREL), Golden, CO.

McAllister ML, Venugopal V and Borthwick AGL (2017) Wave directional spreading from point field measurements. *Proceedings of the Royal Society A* **473**: 20160781.
Morison JR, O'Brien MP, Johnson JW and Schaaf SA (1950) The force exerted by surface waves on piles. *Journal of Petroleum Technology* **189**: 149–154.

Nielsen AW, Schlütterer F, Sørensen JVT and Bredmose H July 2012 Wave loads on a monopile in 3d waves. In *Proceedings of the ASME 2012 31st International Conference on*

Ocean, Offshore and Arctic Engineering - OMAE2012, American Society of Mechanical Engineers, Rio de Janeiro, Brazil.

Papoulis A (1991) *Probability, Random Variables, and Stochastic Processes*. 3rd edn., McGraw-Hill, Inc., United States.

Sarpkaya T (2006) *Hydrodynamic Damping*. *Technical Report Technical report No. NPS/TS-0406*, Naval Postgraduate School, Monterey, CA 93943.

Sarpkaya T and Isaacson M (1981) *Mechanics of wave forces on offshore structures*. Van Nostrand Reinhold Co.

Schløer S, Bredmose H and Bingham HB (2011) Irregular wave forces on monopile foundations. effect of full nonlinearity and bed slope. In *Proceedings of the ASME 30th 2011 International Conference on Ocean, Offshore and Arctic Engineering*, vol. 5, American Society of Mechanical Engineers, pp. 581–588.

Sperstad IB, Halvorsen-Weare EE, Hoffman M, Nonas LM, Stalhane M and Wu M (2014) A comparison of single- and multi-parameter wave criteria for accessing wind turbines in strategic maintenance and logistics models for offshore wind farms. In *EERA DeepWind' 2014, 11th Deep Sea Offshore Wind R&D Conference*, vol. 53, pp. 221–230.

Sumer BM and Fredsøe J (2006) *Advanced Series on Ocean Engineering - Hydrodynamics Around Cylindrical Structures*, vol. 26. World Scientific Publishing Co. Pte. Ltd.

Swan C and Sheikh R (2014) The interaction between steep waves and a surface-piercing column. *Philosophical Transactions of the Royal Society A: Mathematical, Physical and Engineering Sciences* **373(2033)**.

Taylor M, Ralon P and Ilas A June 2016 *The Power to Change: Solar and Wind Cost Reduction Potential to 2025*. *Technical report*, International Renewable Energy Agency (IRENA).

van Bussel GJW, Henderson AR, Morgen CA, Smith B, Barthelmie R and Argyriadis K December 2001 State of the art and technology trends for offshore wind energy: Operation and maintenance issues. In *Proceedings of offshore wind energy special topic conference*, Brussels, Belgium.

Wang CY 1968 On high frequency oscillating viscous flows. *Journal of Fluid Mechanics* **32**: 55–68.

Yang C and Ertekin RC February 1991 Numerical simulation of nonlinear wave diffraction by a vertical cylinder. *Journal of Offshore and Arctic Engineering* **114(1)**: 34–44.

Zdravkovich M (1997) *Flow Around Circular Cylinders. Volume 1: Fundamentals*. OUP Oxford.

Accepted manuscript doi:
10.1680/jmaen.2018.16

Table 1. Parameters used for the sea state simulation including mesh elements and total CPU time

Date	Min. T (s)	Max. T (s)	T_p (s)	Peak Energy (m^2Hz)	H_s (m)	No. Elements	CPU
Sept. 2015	2.86	13.19	8.69	0.214	0.75	2.8M	31 h 40 m
Dec. 2015	2.00	21.74	8.11 & 2.61	Pk1: 0.079 Pk2: 0.070	0.52	3.3M	58 h 35 m
Mar. 2016	2.00	13.28	7.50	0.533	0.89	2.6 M	59 h 26 m
June 2016	1.67	13.33	8.35	0.172	0.41	3.3M	83 h 31 m

Table 2. Significant wave heights for Teesside Farm covering all seasons over the 2015-2016 year

Date	$H_{s,\infty}$ (m)	$H_{s,\mathrm{D}}$ (m)	$H_{s,\mathrm{S}}$ (m)	$H_{s,\mathrm{N}}$ (m)
Sept. 2015	0.53	0.39	0.34	0.32
Dec. 2015	0.54	0.42	0.32	0.30
March 2016	0.89	0.63	0.59	0.56
June 2016	0.49	0.35	0.29	0.22

Table 3. Non-dimensional parameter values for Teesside Farm covering all seasons over the 2015-2016 year.

Date	KC	β	C_d	C_m
Sept. 2015	0.24	2.89×10^6	0.08	2.04
Dec. 2015	0.23	3.28×10^6	0.24	2.00
March 2016	0.35	3.48×10^6	0.05	2.04
June 2016	0.21	2.87×10^6	0.07	2.04

Table 4. Peak force values for Teesside Farm covering all seasons over the 2015-2016 year. Units are given in GN / Hz^2

Date	$m_0(F_M)$	$m_0(F_D)$	$m_0(F_S)$	$m_0(F_N)$
Sept. 2015	5.84	5.29	5.27	4.37
Dec. 2015	1.98	1.03	1.27	1.45
March 2016	6.15	5.29	5.27	4.37
June 2016	0.81	1.20	1.08	0.79

Accepted manuscript doi:
10.1680/jmaen.2018.16

Figure 1. Illustration of the CTV-Monopile System, indicating wave and vessel motor force directions

Figure 2. Location of Teesside Offshore Wind Farm; Image provided by EDF Energy Renewables

Figure 3. Mesh with monopile present, magnified region illustrates downstream grading close to the cylinder walls

Figure 4. Free surface elevation time series comparisons between the undisturbed surface elevation, η_∞, numerically predicted surface elevation η_S, where mesh 1 uses 75 cells per wavelengthand mesh 2 uses 105 cells per wavelength, and diffraction solution η_D.

Figure 5. Comparison between numerical predictions and linear analytical solutions of in-line wave force time histories for progressive, regular waves of period T = 8 s and height H = 1 m. The subscript M represents the solution to the Morison equation, subscripts S are the numerical predictions for each mesh (mesh 1 has 75 cells per wavelength and mesh 2 has 105 cells per wavelength) and the analytical diffracted solution is represented by the subscript D.

Figure 6. Paraview visualization of wave diffraction pattern and wake formation in the vicinity of a large-diameter surface-piercing cylinder representing a turbine monopile using wave input data from March 2016

Figure 7. Surface elevation wave spectral density functions for the raw surface displacement data S_η, diffracted wave spectrum $S_{\eta,D}$, numerical wave spectrum with slip boundary condition $S_{\eta,S}$, and numerical wave spectrum with no-slip boundary condition, $S_{\eta,N}$. Figures display wave spectrum data for (a) Autumn, (b) Winter, (c) Spring and (d) Summer.

Figure 8. Predicted horizontal and vertical velocity component spectra for (a) Autumn, (b) Winter, (c) Spring and (d) Summer at Teesside Offshore Wind Farm, southern North Sea. The subscript ∞ indicates the undisturbed spectrum, D the diffracted spectrum, S and N are the numerical spectra obtained using slip and no-slip boundary conditions.

Figure 9. Predicted force spectra for (a) Autumn, (b) Winter, (c) Spring and (d) Summer at a site in the southern North Sea

Accepted manuscript doi:
10.1680/jmaen.2018.16

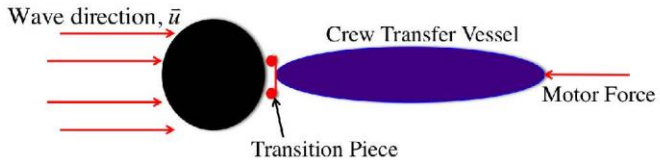

Figure 1. Illustration of the CTV-Monopile System, indicating wave and vessel motor force directions

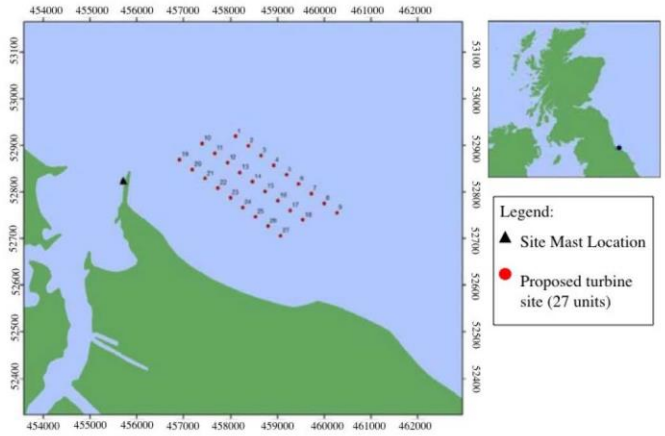

Figure 2. Location of Teesside Offshore Wind Farm; Image provided by EDF Energy Renewables

Accepted manuscript doi:
10.1680/jmaen.2018.16

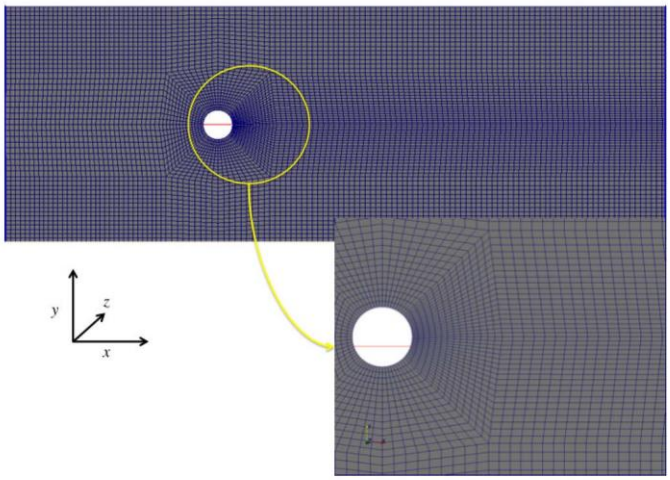

Figure 3. Mesh with monopile present, magnified region illustrates downstream grading close to the cylinder walls

Accepted manuscript doi:
10.1680/jmaen.2018.16

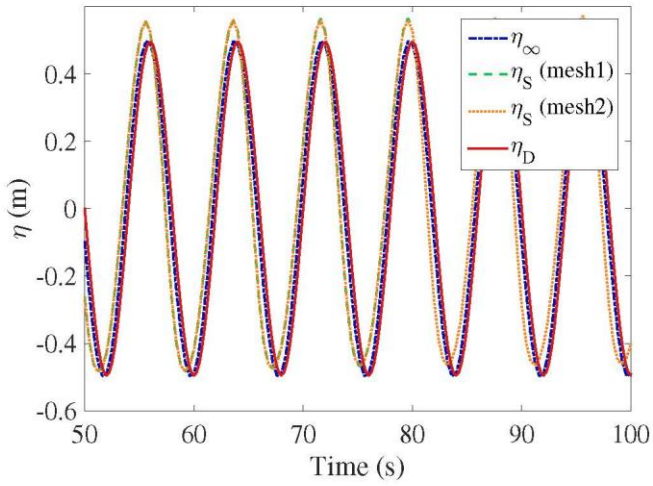

Figure 4. Free surface elevation time series comparisons between the undisturbed surface elevation, η_∞, numerically predicted surface elevation η_S, where mesh 1 uses 75 cells per wavelength and mesh 2 uses 105 cells per wavelength, and diffraction solution η_D.

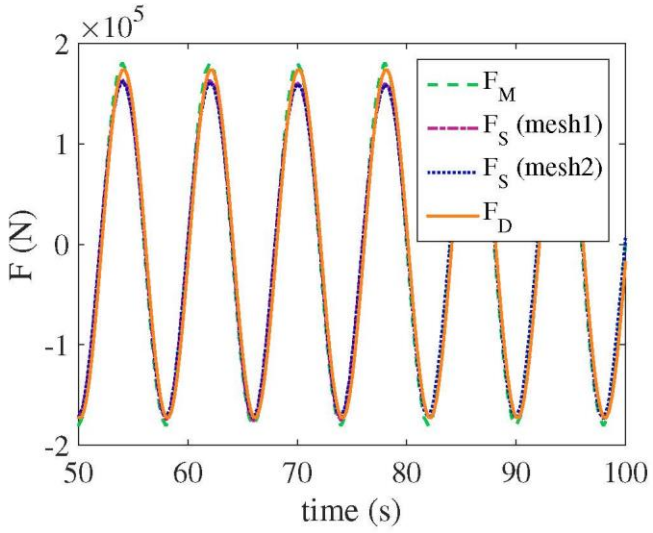

Figure 5. Comparison between numerical predictions and linear analytical solutions of in-line wave force time histories for progressive, regular waves of period T = 8 s and height H = 1 m. The subscript M represents the solution to the Morison equation, subscripts S are the numerical predictions for each mesh (mesh 1 has 75 cells per wavelength and mesh 2 has 105 cells per wavelength) and the analytical diffracted solution is represented by the subscript D.

Accepted manuscript doi:
10.1680/jmaen.2018.16

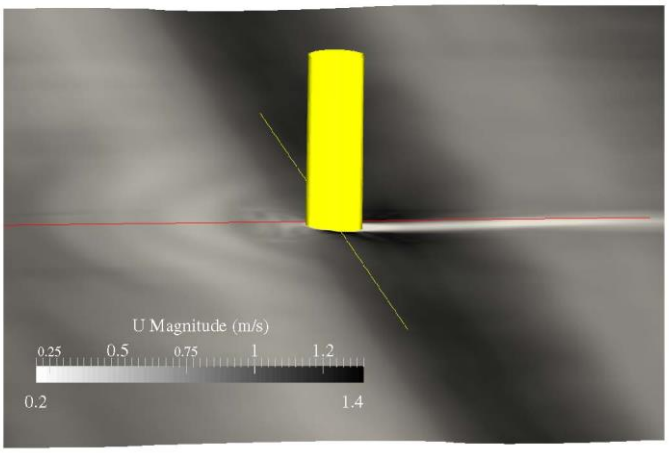

Figure 6. Paraview visualization of wave diffraction pattern and wake formation in the vicinity of a large-diameter surface-piercing cylinder representing a turbine monopile using wave input data from March 2016

Accepted manuscript doi:
10.1680/jmaen.2018.16

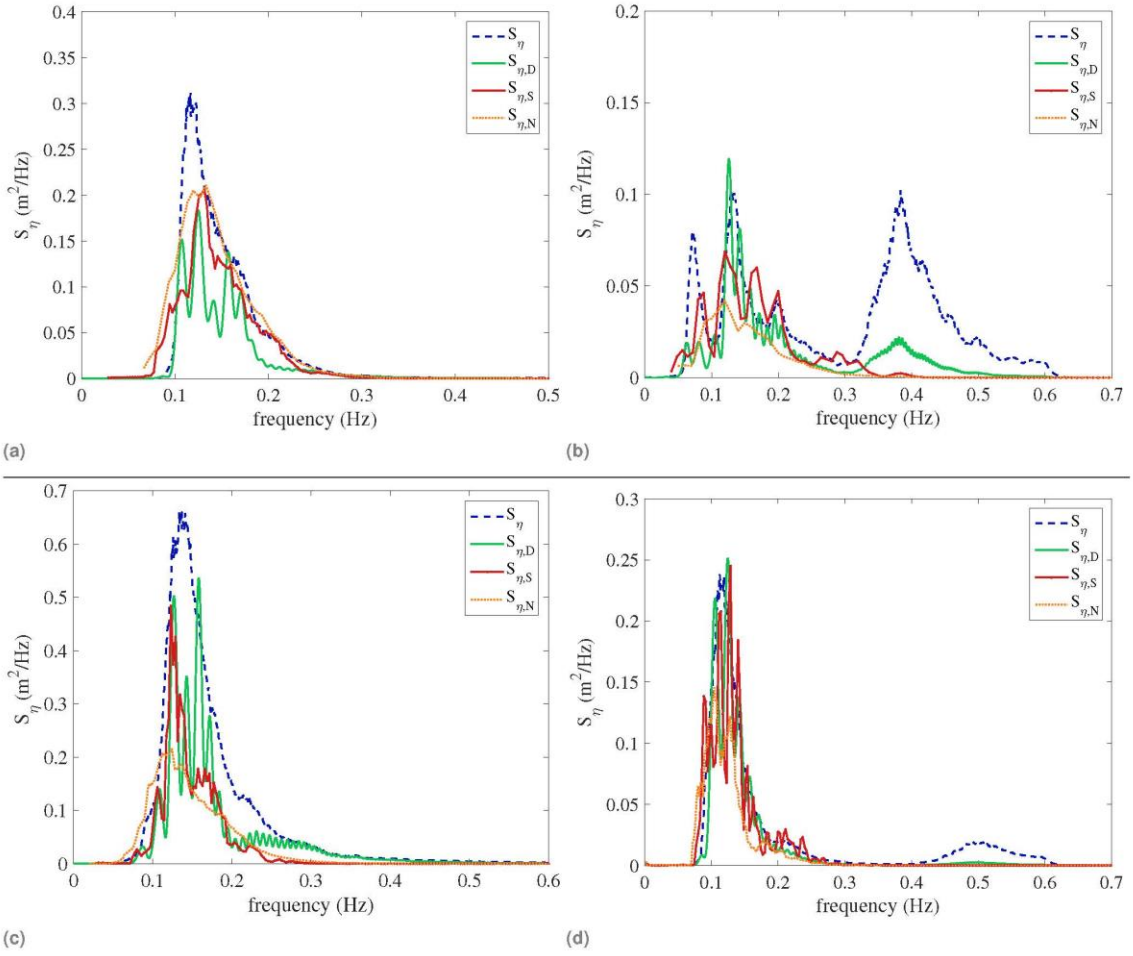

Figure 7. Surface elevation wave spectral density functions for the raw surface displacement data S_η, diffracted wave spectrum $S_{\eta,D}$, numerical wave spectrum with slip boundary condition $S_{\eta,S}$, and numerical wave spectrum with no-slip boundary condition, $S_{\eta,N}$. Figures display wave spectrum data for (a) Autumn, (b) Winter, (c) Spring and (d) Summer.

Accepted manuscript doi:
10.1680/jmaen.2018.16

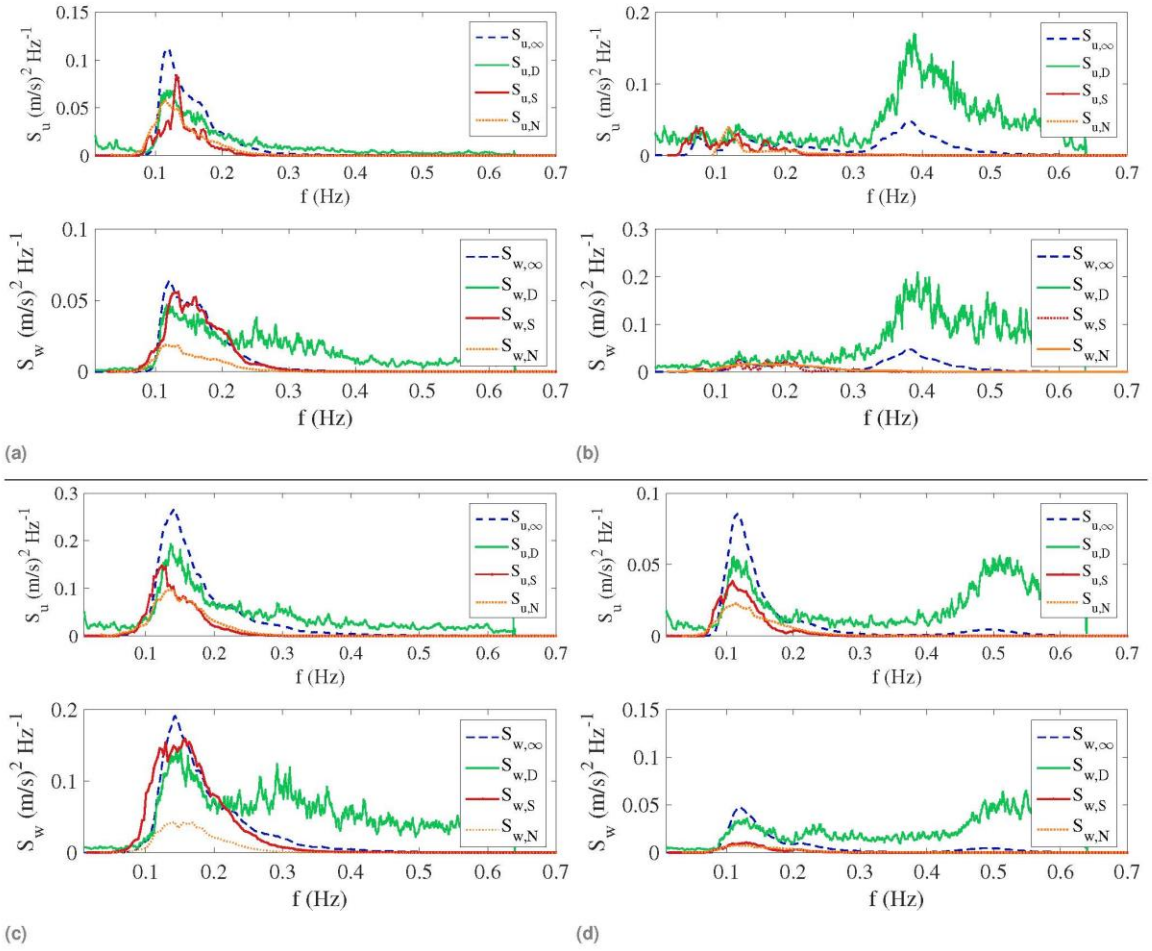

Figure 8. Predicted horizontal and vertical velocity component spectra for (a) Autumn, (b) Winter, (c) Spring and (d) Summer at Teesside Offshore Wind Farm, southern North Sea. The subscript ∞ indicates the undisturbed spectrum, D the diffracted spectrum, S and N are the numerical spectra obtained using slip and no-slip boundary conditions.

Accepted manuscript doi:
10.1680/jmaen.2018.16

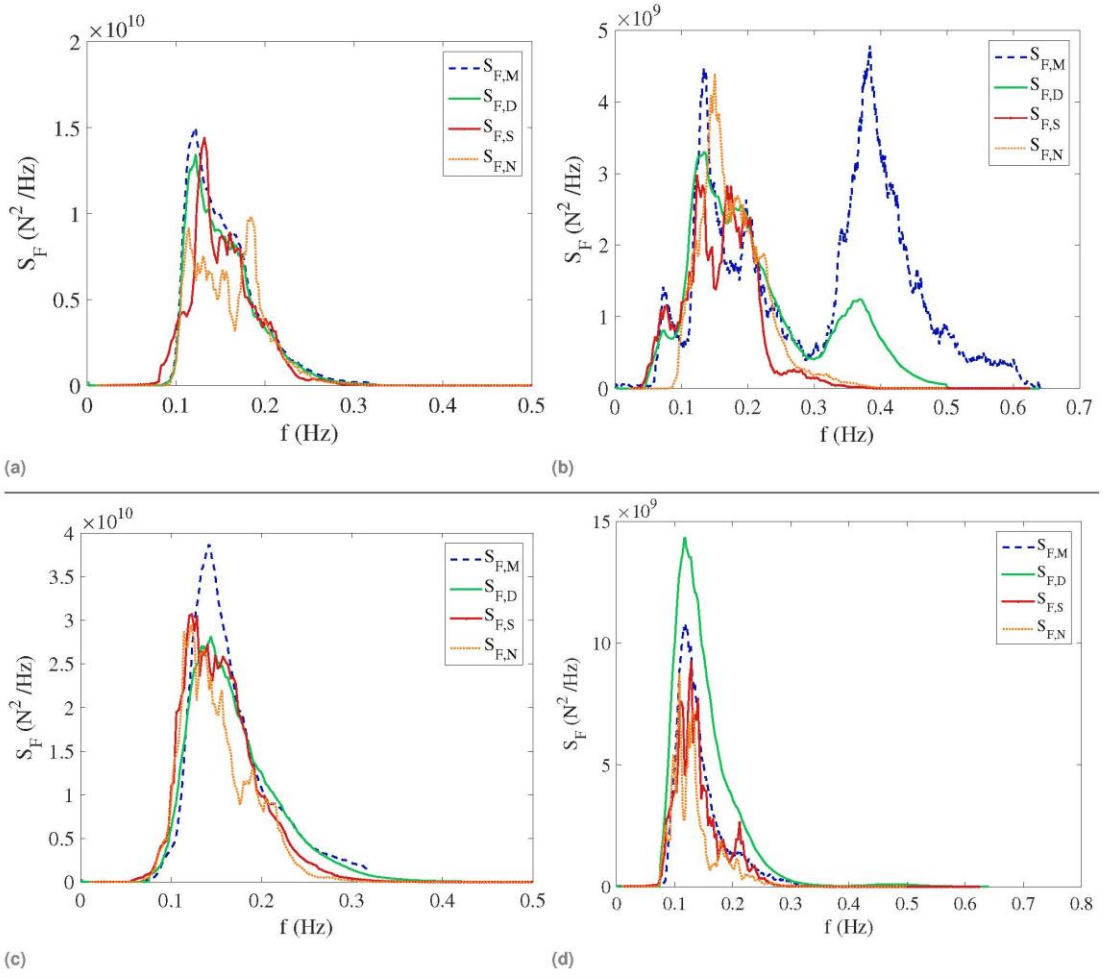

Figure 9. Predicted force spectra for (a) Autumn, (b) Winter, (c) Spring and (d) Summer at a site in the southern North Sea